NUMERICAL EVALUATION OF THE ACCURACY IN THE LOAD SHARING CALCULATION USING STRAIN GAUGES: SUN AND RING GEAR TOOTH ROOT

J. Sanchez-Espiga, A. Fernandez-del-Rincon, M. Iglesias, F. Viadero

Departamento de Ingeniería Estructural y Mecánica, Universidad de Cantabria, Avda. de los Castros s/n 39005 Santander, Spain.

Abstract

This work aims to extend the understanding in the use of strain gauges in the root of the teeth in order to calculate the load sharing in planetary transmissions. Continuing with the numerical analysis of the accuracy of the experimental measurements, this work studies the influence of the placing of strain gauges in the accuracy of the measurements. Thus, the strain gauges are placed in the ring and sun gears. Furthermore, new effects are added to the simulations in order to enhance its realism. Hence, the stiffness in the sun support is varied, as well as the number of planets is raised. Finally, the results show discrepancies between the real load sharing and the measured load sharing, more importantly, these differences prove that the measurements underestimate the load sharing in the transmission, which could be crucial in the durability and certification of such a transmission.

Keywords: Mesh phasing, Wind generators, Load sharing, Strain gauges, Certification

1. Introduction

Mechanical power transmissions are crucial components in many industrial applications. More precisely, among them gear transmissions are vital components in a number of applications, namely, heavy mining [1], vehicles [2], wind generators [3, 4, 5, 6], and aircrafts [7, 8]. Gear transmissions present a wide variety of possible solutions to the same problem. More precisely, this

work focuses on planetary gears. This kind of transmission provides numerous advantages compared to other options such as their compactness, higher power, robustness, and different transmission ratios varying its configuration, among others.

In the study of planetary gears, virtual modelling has been a useful tool aiming to reduce the cost of the study and reaching high standards in terms of realism. Thus, a number of models have been developed in the last decades, improving the realism and including a number of new effects in the simulations as the problems in the industry developed. Thus, lumped-parameter models were the first approach to the computation of planetary gear modelling [9, 10, 11, 12, 13, 14, 15, 16, 17]. Afterwards, hybrid proposals [4, 18, 19, 20, 21] started to be developed in order to improve the accuracy of the models, widen the scope of its aplicability and reduce the computational cost. In this last group, the model employed for these simulations is included [22].

Despite the realism reached in the models, experimental works are still a highlight in the context of research in planetary gears. In the last decades, numerous experimental works have been developed to characterize the planetary transmissions behaviour. In order to study the dynamical behaviour of a planetary transmission diverse techniques are appropriate, accelerometry [23, 24, 25, 26], acoustic emission [26, 27], and acoustic intensity [28] among others. Another technology that is employed for experimental studies is extensometry, which allows to calculate the stains in the root tooth and the amount of load in such tooth [29, 30, 31]. One of the most common applications is the use of extensometry to address the load sharing in a planetary transmission , however, the most appropriate placing for the strain gauges is still undetermined, some authors tried in the sun gear [32], others in the ring gear [17, 33, 34, 35], and more recently, in the planet pins [36, 37, 38, 39].

Focusing on a precise application of a planetary transmission, wind generators incorporate a multistage planetary transmission multiplier. In this application the standard is set by [40], which in its section regarding the load sharing and the mesh load factor (K_γ) advises using strain gauges to calculate the mentioned factor.

Thus, the present work focuses on the study of the accuracy of the experimental measurements of the load sharing by using strain gauges. The motivation behind this new work comes from the discrepancies presented in [32, 41] between the real and the measured load sharing. Thus, this new work proposes a numerical study to assess the accuracy of using strain gauges

both in the root of the sun and ring gear teeth in order to calculate the load mesh factor in a planetary transmission. The accuracy of these measurements is of upmost importance given their direct connection with the validation and certification of the good performance of any planetary gearboxes. Thus, this study aims to compare the accuracy of the measurements depending on the location of the gauges, which as mentioned before is still undetermined and different locations are considered valid. Moreover, the scope of studied transmissions is extended by increasing the number of planets, which proved to be crucial in the impact of different effects such as errors [15, 16, 34, 42, 43, 44, 45]. Afterwards, the stiffness in the sun support will be varied in a wide number of solutions and studied only for 5 planet transmissions, keeping a realistic configuration with an odd number of planets and avoiding the self-balancing effect inherent to 3-planet transmissions with a floating sun.

Finally, this work will be composed by an starting Section 2 where the already existing employed model is described. In every subsection along Section 2 various aspects that have been modified in the model, in order to face the new study, are addressed. Then, Section 3 gathers the cases of study considered in the context of this work. Afterwards, in Section 4 the results to those cases are shown and analysed. Finally, Section 5 compiles the conclusions fruit of this study.

2. Modelling

A semi-analytical 2-D planetary gear model [22] is modified in order to obtain the deformations in the root arc between consecutive teeth both in the sun and ring gears. The presented model consists in a semi-analytical formulation that combines finite-element(FE) models, together with the Weber-Banashek approach for the Hertzian resolution of the local contact between gears.

Thus, the model defines the geometry of the wheels and a set of FE models, which will be described in more detail in Section 2.1. By using these models the linear part of the contact problem can be solved by establishing the stiffness of the wheels and the teeth from their response to the application of a unitary force along the active flank. Then, the Weber-Banashek formulation takes a Hertzian approach to solving the local contact problem between the active flanks of pairs of teeth in contact. This part is nonlinear. By using an iterative method the contact problem can be solved by com-

bining the linear and non-linear problems and using the local FE model to eliminate the distortion due to the point force in the model, as it will be seen in Section 2.1.

Once the contact problem is solved for all the existing contacts, the model solves the balance problem. Given the fact that this is a quasi-static approach without losses, the dynamic effects and the losses due to friction or lubrication are not considered. Thus, there will be a balance between the input and output torque, as well as a balance in torque in each of the planets, considering the contacts with the sun and ring. Then, in the case of the variation in the sun support stiffness, the balance is extended also to the vectors of the contact forces in the sun and the force that appears in the support as a consequence, which closes the vector system. The latter generates a deflection in the sun shaft to place it into the balance position as seen in [45].

Finally, once all the above is solved, the results can be extracted given the fact that the contacts are located and the contact forces for each teeth are known.

2.1. Finite-element Models

As mentioned above, in this subsection the focus is on the detail of the FE models. Firstly, a number of 2-D global FE models, one for each different wheel, are defined using the partial differential equation toolbox in MATLAB. These models combine a Z number of teeth, which comes from eqn.1, and the body of the gear (Fig.1). For the latter, the guidelines for the back-up ratio included in [46] are considered to determine the size of the shaft mountings. Afterwards, every of these models is meshed with triangular elements where the nodes are located in each vertex. In terms of boundary conditions, each of these models are embedded to the frame in their mounting, which in the sun and planet gears is the inner circle that represents the shaft mounting, in the case of the ring gear this embedding spreads along the periphery of the wheel in its outer diameter.

$$Z = 2 \cdot Ceil(\varepsilon + 1) \tag{1}$$

As far as the local FE model is concerned, it represents the geometry of the teeth flank up to an h depth, as seen in Fig.2. The calculation of this depth is addressed in [22] assuring it being enough to consider the deformations due to the point force. Moreover, this model is also meshed using triangular elements with nodes in the vertexes. Then, the boundary conditions embed

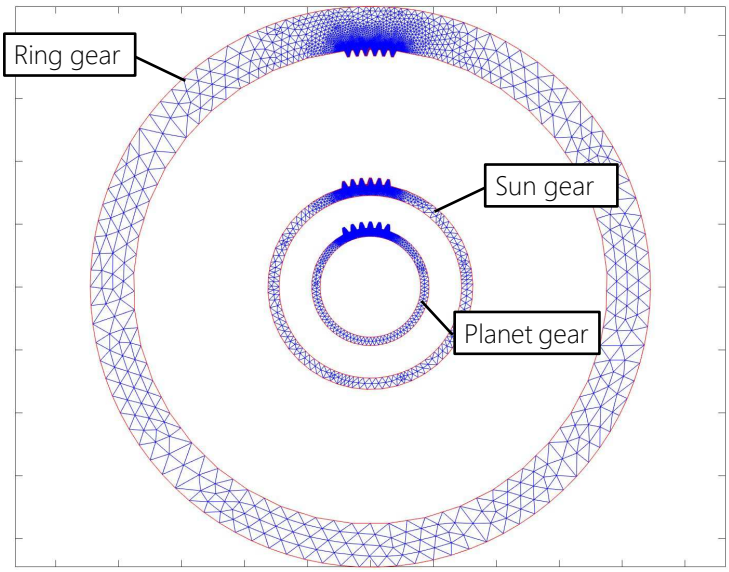

Figure 1: Global FE model for the sun, planet and ring gears

all the geometry that represents the interface between the model and the missing geometry of the tooth, thus, it would be the line along the inner part of the model that follows the flank at an h depth. The purpose of these models, as commented before, focuses on the need to erase the distortion due to the use of point force in any point along the middle tooth flank in the FE model. Hence, the same unitary load is applied in each model with opposite directions. Thus, the overlap principle provides the deflections in the body of the gear and the teeth due to the application of a unitary load in any position along the flank of the active tooth, which will always be the $(Z{+}1)/2$ tooth in the FE model.

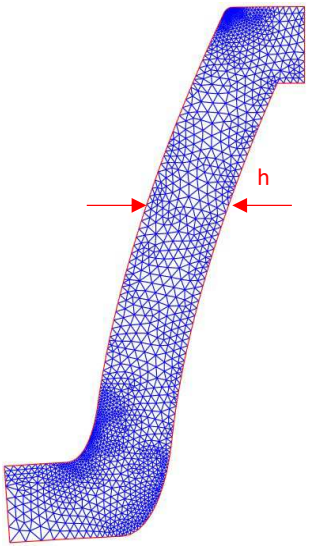

Figure 2: Local FE model for the active flank

2.2. Virtual strain gauges

In this section, the procedure for the definition of a virtual strain gauge presented in [41], for the sun gear, is extended for the geometry of an inner gear, the ring. Thus, a number of nodes in each of the root arcs between consecutive teeth are located and its original coordinates are compiled. Besides, a number of nodes in the root arc immediately before the first tooth, as well as nodes in the root arc after the last tooth. These are identified and their coordinates compiled. In order to identify these nodes for an inner gear, the conditions employed in the sun gear stay, namely:

- The nodes have to belong to the root circumference.

- They must be in the root arc that connects the trochoids of consecutive teeth.

- At the first and last teeth the nodes belong to the root circumference and are the closest to the trochoid.

The nodes identified in each wheel, following the previous conditions, are shown in Fig.3 & Fig.4.

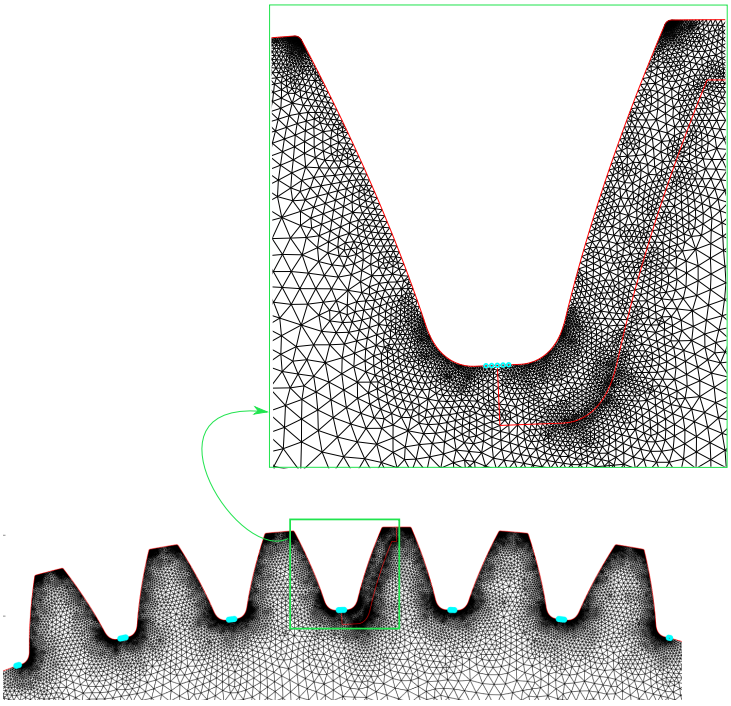

Figure 3: FE model of the sun gear and detail of the nodes (in blue circles)

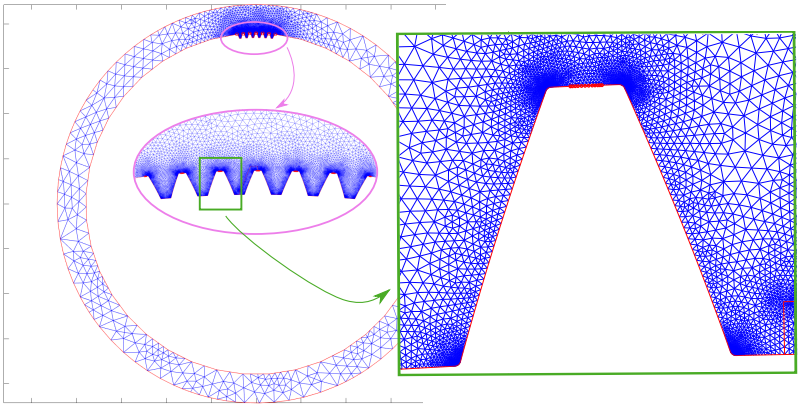

Figure 4: FE model of the ring gear and detail of the nodes (in red circles)

The selection of nodes along the root arc is justified by three reasons, first of all, this location was the one employed in the experimental measurements shown in [32] performed in the sun gear. Secondly, the ease to obtain the

original length of each section and its change due to the contacts. Thirdly, the numerical nature of this study provides the possibility to quantify the slightest deformation and the magnitude of the deformation does not modify the load sharing results given the fact that all of them are obtained by the same procedure. However, experimentally these measurements may be performed in the fillet where the deformations are bigger, which makes it easier to be acquired by the strain gauge.

2.3. Deformations and contact sequence

Once the nodes are selected, the next step consists in managing the information that can be extracted from the FE models. Therefore, as commented before, the global FE models are subjected to a series of load cases, where a unitary force is applied at a different location along the active flank. This flank is always the left flank in the $(Z/2)+1$ tooth in the model, as seen in the several cases shown in Fig.5.

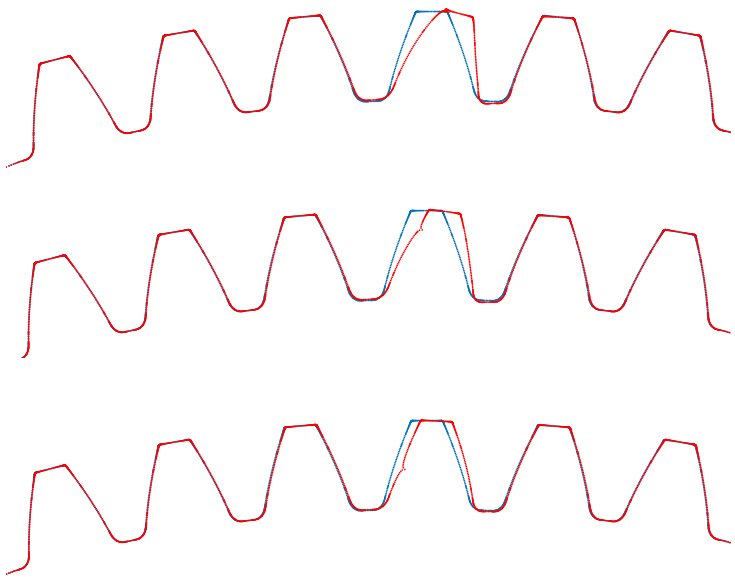

Figure 5: Several load cases for the external contact in the sun FE model represented by its profile: unloaded (blue), loaded (red)

Hence, the initial coordinates of the nodes, previously selected, will provide their original position. After applying that unitary force, these nodes will change its position, both globally and relatively to the rest of the nodes, as shown in more detail in [41]. In order to obtain the length of any noded section in the initial or loaded configuration, the expression used is eqn.2.

$$L_i = \sqrt{N_{i,j}^2 + N_{i,j+1}^2} \tag{2}$$

Where the subindex j refers to the number of node in the i noded section.

Then, the deformation in each section of nodes can be calculated as the difference between the length in the noded sections in the original (L_{oi}) and the loaded (L_i) configurations, as expressed in eqn.3. The subindex i refers to the number of the noded section.

$$\Delta L_i = L_i - L_{oi} \tag{3}$$

Thus, calculating this ΔL_i for each noded section, the deformation in every root arc will be known. Therefore, in order to obtain the deformations on the strain gauge located between a pair of teeth in the sun or ring gear is just a matter of managing the already existing information. In spur gears, there will be scenarios of single or double contact normally, thus, in the cases of single contact just the deformation of one noded section will be of interest. However, in the double contact scenario, the noded sections of interest will be two, and the deformations results will be overlapped.

In order to manage the deformation information, the focus is on the relative positioning between the real contact and the strain gauge. Thus, this positioning must be the same in the FE model. In the FE model the contact is always in the $(Z/2)$+1 tooth. Then, as seen in Fig.6 the relative positioning of the contacts in each scenario determines the noded section of interest and the deformations to consider. Thus, for the example shown, a single contact in the first tooth generates a compression in the strain gauge that is equal to the one experienced in the S7 of the FE model. Moreover, the deformation in the S7 section is multiplied by the module of the contact force, given the fact that the load in the FE model is unitary. Then, for a scenario with a double contact, the overlap principle is applied and the deformations in two different noded sections are considered.

In Fig.6 the strain gauge appears as a red thick segment, then, a color code has been used to identify each load case and to ease the understanding of this crucial diagram. Thus, the color employed in the real contact scenario

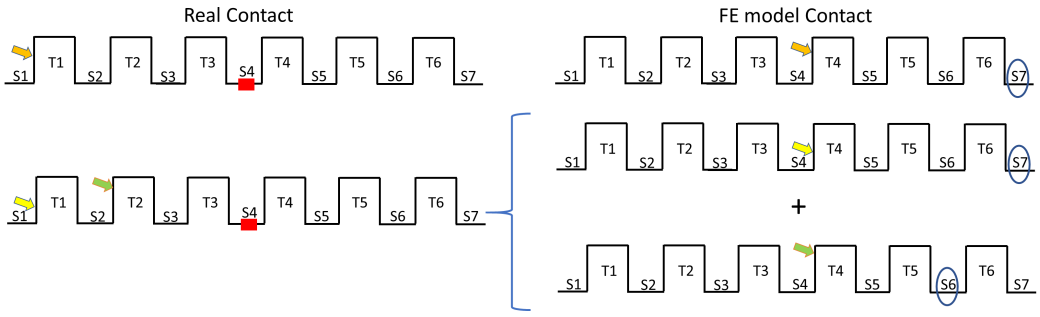

Figure 6: Relative positioning of the contact in the real and simulated situations

corresponds to the FE model contact analogy. The teeth are identified by T_i and the noded sections by S_i. Besides, it is possible to see that with the change of tooth in the real contact the section of interest for the deformations changes accordingly.

Finally, it is relevant to point out the fact that the sequence of contacts is different for the sun and the ring gear, but the procedure followed is analogous.

2.4. Calculation of the K_γ

In the context of gearboxes for wind generators, the IEC 61400 [40] establishes the threshold value of the mesh load factor as a requirement to obtain the certification of these gearboxes, also taken as reference in [47]. These thresholds for the K_γ depending on the number of planets are gathered in Tab.1.

Table 1: Mesh load factor threshold

Number of planets	3	4	5	6	7
K_γ	1.1	1.25	1.35	1.44	1.47

In order to calculate this value, in the present work, two different strategies have been employed. Firstly, the calculation of the real load sharing in the model is performed by using the load sharing ratio (LSR), previously presented in [22, 41]. The definition of the LSR corresponds to the relative amount of load in a planet in comparison to the total load in the transmission. Thus, eqn.4 presents the analytical expression to obtain the LSR in a planetary transmission.

$$LSR_s = \frac{F_s}{\Sigma_{t=1}^{N} F_t} \tag{4}$$

Where F_s refers to the amount of load in the each planet and F_t the load in each planet as part of the summation of total load in the system. The latter could be substituted by the input torque, given the lack of losses and dynamical effects in the simulations.

Secondly, aiming to calculate the load sharing in the transmission from the deformations in the strain gauges, the strain gauge load ratio (SGLR) is defined. This refers to the relative peak-to-peak value obtained in the deformations of a strain gauge due to the contact with any planet, in comparison to the summation of every peak-to-peak values due to the contacts with every planet in a complete meshing cycle. The analytical definition of the SGLR is presented in eqn.5

$$SGLR_s = \frac{X_{sp-p}}{\Sigma_{t=1}^{N} X_{tp-p}} \tag{5}$$

In eqn.5 X_{sp-p} refers to each peak-to-peak value masured by the strain gauge in the contact with each planet. As done before in eqn.4 X_{tp-p} the subindex t is used as an auxiliar subindex to refer to the same peak-to-peak value, but as part of the summation of all the peak-to-peak values in the contacts with every planet.

Finally, the mesh load factor can be obtained both from the LSR and the SGLR by dividing the obtained value by the ideal load sharing value, which is determined by the number of planets N being 0.333 for 3 planets and 0.2 for 5. Also, hereinafter, the mesh load factor that will be considered of importance will be the ones that represent an overload in a given planet. From the durability point of view, the mesh load factor set by the underloaded planets play an unimportant role. Thus, eqn.6 & eqn.7 are employed to calculate the mesh load factor from the LSR and SGLR, the latter for any of the modelled locations for the strain gauge.

$$K_{\gamma LSR} = max(\frac{LSR_i}{LSR_{ideal}}) \tag{6}$$

$$K_{\gamma SGLR} = max(\frac{SGLR_s}{LSR_{ideal}}) \tag{7}$$

For the load sharing and K_γ calculated from the deformation in the strain gauges, the results for the sun and ring gears will be differentiated by the subindex su or ri respectively.

3. Cases of study

In the first place, a couple of planetary transmissions are defined in order to present analogous configurations, in terms of geometry, both for Equally Spaced In-phase (ESIP) and Equally Spaced Sequentially Phased (ESSP) transmissions. Thus, in the transmissions gathered in Tab. 2 the number of teeth for every wheel are compiled. These numbers of teeth are useful for transmissions between 3 - 6 planets, which can be confirmed by verifying the requirements gathered in [25, 43].

Table 2: Number of teeth for each gear in the considered transmissions

	Z_r	Z_p	Z_s
ESIP	165	44	75
ESSP	166	45	74

Then, the profile of every teeth are defined following the geometrical specifications gathered in Tab.3. The inclusion of a tip rounding arc helps to avoid the possible contact at the tip of the tooth, and thus, the dramatic change in the meshing stiffness, which affects the convergence in the numerical model.

Table 3: Geometrical specifications of the teeth profiles

Parameter	Value
Module (mm)	4.5
Pressure angle (°)	20
Adendum (mm)	4.5
Deddendum (mm)	4.5
Tip rounding arc radius (mm)	0.225
Contact ratio (sun-planet)	1.295
Contact ratio (planet-ring)	1.397

After validating the well-functioning of the system with ideal transmissions, with no errors, a series of tangential pinhole position errors will be included. These errors are gathered in Tab.4, however, the size of the tangential pinhole position errors will vary due to the change in the stiffness of the sun support, more flexibility widens the range of admissible tangential pinhole error. In the more stiff transmissions there is a loss of contact in one of the planets for smaller tangential error. Even though the errors are not the same for each scenario, they will describe the same tendencies , so it will be possible to compare and extract conclusions from the results presented. The variation of the stiffness in the sun support will be only performed for 5-planet transmissions in order to avoid the self-balancing effect inherent to 3-planet transmissions with a floating sun, as seen in [45].

Table 4: Compilation of the studied scenarios

Sun support stiffness (N/m)	Tangential error (e_t)					
Fixed	0 μm	0.625 μm	1.25 μm	1.875 μm	2.5 μm	3.125 μm
1e9	0 μm	1.25 μm	2.5 μm	3.75 μm		
1e8	0 μm	1.25 μm	2.5 μm	3.75 μm	5 μm	
1e7	0 μm	1.25 μm	2.5 μm	3.75 μm	5 μm	6.25 μm
1e6	0 μm	1.25 μm	2.5 μm	3.75 μm	5 μm	6.25 μm

4. Results and discussion

Hereinafter, the results to all the cases of study proposed previously are gathered. Firstly, the simulations of the strain gauge deformations in the sun root, presented in [41], are compared with the new method employed in the root of the ring gear teeth. Previously, these simulations were performed in 3-planet transmissions, however, in this work this is extended to 5-planet transmissions. Afterwards, this 5-planet transmissions will include also various stiffnesses in the sun gear support, as well as several tangential pinhole position errors in the planet 1.

4.1. Comparison between ring and sun measurements

Firstly, ideal transmissions are simulated looking for validation of the good performance in the model. For an ideal ESIP transmission without any error the load is perfectly balanced among every planet, as seen in Tab.5 & Tab.6. However, in ESSP transmissions this does not happen (Tab.7 & Tab.8), due to the effect of the mesh phasing. Besides, the mesh phasing includes an inherent error in the results of the measured load sharing [41].

Table 5: Results of load sharing for ESIP 3-planet transmission

	Planet 1	Planet 2	Planet 3
LSR	0.333	0.333	0.333
$SGLR_{su}$	0.333	0.333	0.333
$SGLR_{ri}$	0.333	0.333	0.333

Table 6: Results of load sharing for ESIP 5-planet transmission

	Planet 1	Planet 2	Planet 3	Planet 4	Planet 5
LSR	0.2	0.2	0.2	0.2	0.2
$SGLR_{su}$	0.2	0.2	0.2	0.2	0.2
$SGLR_{ri}$	0.2	0.2	0.2	0.2	0.2

Thus, in the case of ESSP transmissions for both the sun and ring gear measurements, there is a discrepancy between the real load sharing (LSR) and the load sharing obtained from the measurements, as seen in Tab.7 & Tab.8. These discrepancies are totally related to the asynchronous nature of the measurements in comparison to the calculation of the real load sharing, as seen in [41]. This explanation applies equally to the sun and ring gear placements, delivering wrongly-ideal results with both measurements.

Table 7: Results of load sharing for ESSP 3-planet transmission

	Planet 1	Planet 2	Planet 3
LSR	0.363	0.363	0.363
$SGLR_{su}$	0.333	0.333	0.333
$SGLR_{ri}$	0.333	0.333	0.333

Table 8: Results of load sharing for ESSP 5-planet transmission

	Planet 1	Planet 2	Planet 3	Planet 4	Planet 5
LSR	0.2182	0.2181	0.2181	0.2181	0.2181
$SGLR_{su}$	0.2	0.2	0.2	0.2	0.2
$SGLR_{ri}$	0.2	0.2	0.2	0.2	0.2

Afterwards, the tangential pinhole position errors specified in Tab.4 are included in the pinhole of planet 1, for the 5-planet transmissions. Thus, an imbalance is generated. In the Tab.9 & Tab.10, the results of K_γ obtained for the LSR and both SGLR are gathered. The imbalance introduced by the tangential error affects differently the results due to the mesh phasing, always remembering that the LSR shows the real load sharing.

Table 9: K_γ for ESIP 5-planet transmission

Error size (μm)	0	0.625	1.25	1.875	2.5	3.125
$K_{\gamma LSR}$	1	1.0465	1.093	1.1435	1.1845	1.229
$K_{\gamma SGLR_{su}}$	1	1.0335	1.0625	1.091	1.1185	1.1465
$K_{\gamma SGLR_{ri}}$	1	1.028	1.056	1.084	1.1115	1.139

Table 10: K_γ for ESSP 5-planet transmission

Error size (μm)	0	0.625	1.25	1.875	2.5	3.125
$K_{\gamma LSR}$	1.0905	1.1305	1.1655	1.201	1.239	1.276
$K_{\gamma SGLR_{su}}$	1	1.0365	1.0705	1.1045	1.1405	1.175
$K_{\gamma SGLR_{ri}}$	1	1.0865	1.123	1.1555	1.1855	1.2015

From these results, it is relevant to point out the fact that the measurements underestimate the imbalance created by the tangential pinhole position errors in any of the cases. Besides, the inaccuracy in the K_γ grows with the increment of the tangential pinhole position error. For the ESSP

transmission, the measurements in the ring are over the ones in the sun, which is completely the opposite to the situation in the ESIP transmissions. Therefore, it seems that the error in these measurements does not depend on the placement of the strain gauge, at least in the considered scope.

4.2. Influence of the stiffness in the sun support

In this section, the work is extended by including the effect of the variable stiffness in the sun support. Together with such effect, it is relevant to vary the size range of the tangential errors accordingly. As done before, this study is focused on 5-planet transmissions, looking for avoiding the self-balancing effect inherent to 3-planet transmissions with a floating sun gear.

Thus, in the next tables the series of results for the cases of study proposed before are gathered. Hereinafter, the tables within Tab.11 to Tab.18 present the K_γ results for ESIP and ESSP transmissions with the proposed sun support stiffnesses. In the first case, with 1e9 N/m stiffness (Tab.11 & Tab.12), the results present some similarities with the sun-fixed simulations. However, for the same size in the tangential error, the configuration with lower stiffness in the support shows worse K_γ. Hence, the added freedom in the translation of the sun gear does not improve the load sharing.

Table 11: K_γ for ESIP 5-planet transmissions with tangential errors and 1e9 N/m stiffness in the sun

Error size (μm)	0	1.25	2.5	3.75
$K_{\gamma LSR}$	1	1.118	1.2355	1.351
$K_{\gamma SGLR_{su}}$	1	1.0805	1.1545	1.2285
$K_{\gamma SGLR_{ri}}$	1	1.067	1.134	1.2

Table 12: K_γ for ESSP 5-planet transmissions with tangential errors and 1e9 N/m stiffness in the sun

Error size (μm)	0	1.25	2.5	3.75	5
$K_{\gamma LSR}$	1.11	1.203	1.2814	1.3578	1.4323
$K_{\gamma SGLR_{su}}$	1	1.0846	1.1695	1.255	1.3361
$K_{\gamma SGLR_{ri}}$	1	1.088	1.1615	1.2382	1.3136

Comparing the ESIP and ESSP transmission for the same support stiffness (Fig.7 & Fig.8), it is visible how the $K\gamma$ is bigger in the ESSP configuration than in the ESIP. However, the growth of the $K\gamma$ with the tangential pinhole position error is faster in the ESIP than in the ESSP transmission. In both scenarios it is visible that the measurements are inaccurate and underestimate the load in the planet that determines the $K\gamma$.

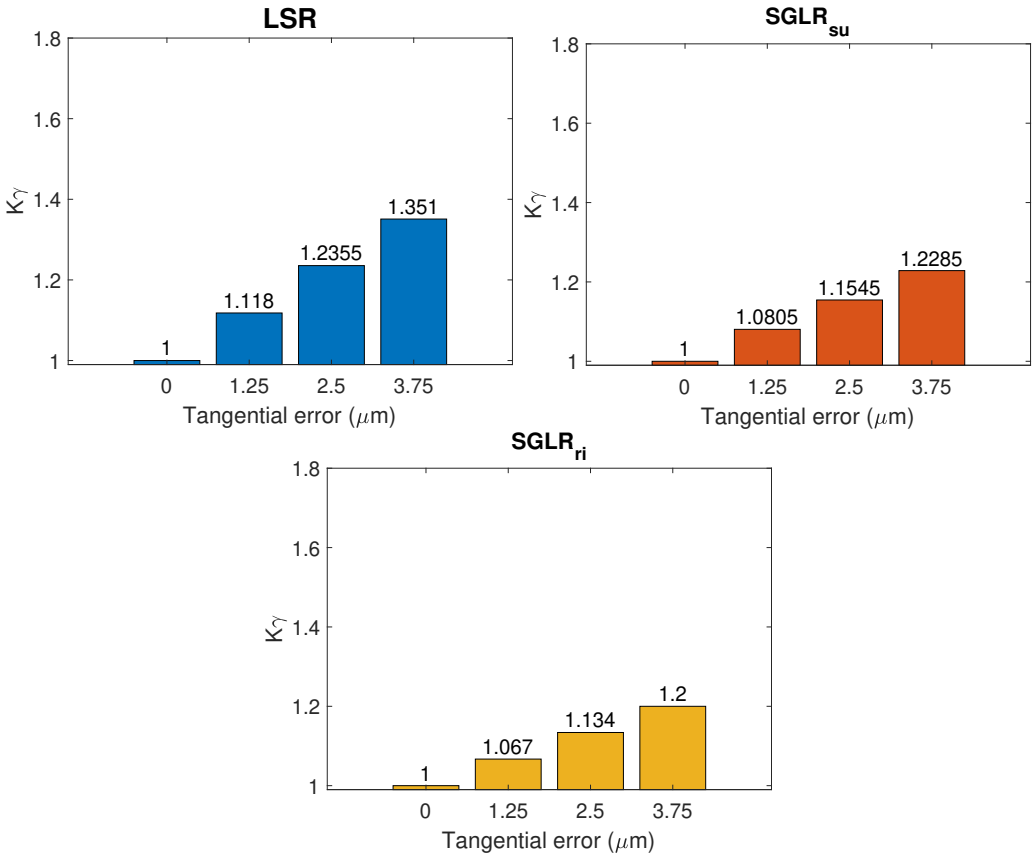

Figure 7: $K\gamma$ for 5-planet ESIP and 1e9 N/m stiffness in the sun support

This stands for the 1e9 & 1e8 N/m stiffness configurations. However, the results for the 1e8 N/m stiffness (Tab.13 & Tab.14) and a 5 μm error show a change in the tendency of the $K\gamma$. The $K\gamma$ becomes higher in ESIP transmission than in the ESSP, which will be seen in more depth in the following scenarios (Tab.15, Tab.16, Tab.17 & Tab.18).

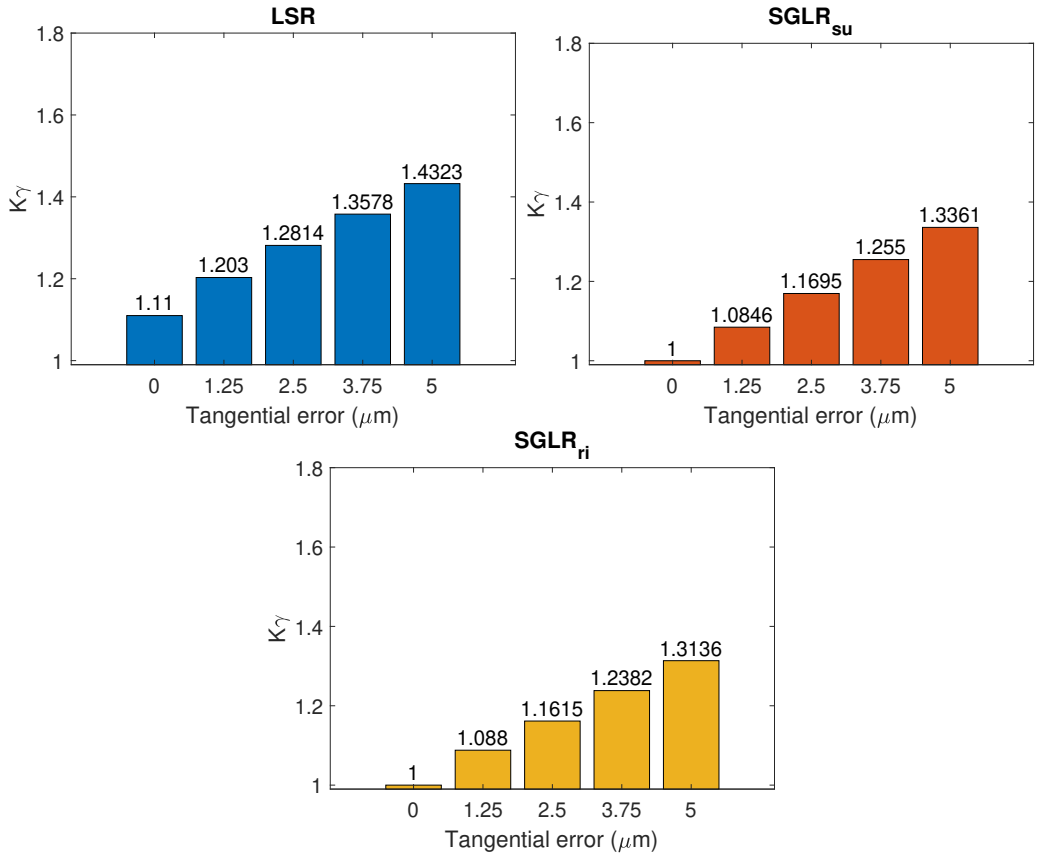

Figure 8: $K\gamma$ for 5-planet ESSP and 1e9 N/m stiffness in the sun support

Table 13: K_γ for ESIP 5-planet transmissions with tangential errors and 1e8 N/m stiffness in the sun

Error size (μm)	0	1.25	2.5	3.75	5
$K_{\gamma LSR}$	1	1.1445	1.2885	1.4325	1.575
$K_{\gamma SGLR_{su}}$	1	1.104	1.201	1.298	1.391
$K_{\gamma SGLR_{ri}}$	1	1.085	1.1695	1.2545	1.339

Table 14: K_γ for ESSP 5-planet transmissions with tangential errors and 1e8 N/m stiffness in the sun

Error size (μm)	0	1.25	2.5	3.75	5	6.25
$K_{\gamma LSR}$	1.135	1.248	1.35	1.4465	1.543	1.638
$K_{\gamma SGLR_{su}}$	1	1.1012	1.203	1.305	1.4065	1.5075
$K_{\gamma SGLR_{ri}}$	1	1.088	1.193	1.282	1.375	1.47

In the following scenarios, the sun support is loosened, however, the load sharing behaviour gets worse, contrary to what can be previously supposed considering the example set by the 3-planet configurations. Thus, the $K_{\gamma LSR}$ results reach significant values, worse with the increase in the flexibility in the sun support. However, in Tab.15 to Tab.18 it is possible to identify a very similar behaviour, proving that the limit to where the stiffness in the support makes a difference has been reached.

On the other hand, in the 1e7 N/m stiffness (Tab.15 & Tab.16) the different growth in the $K\gamma$ changes what was stated before. For small tangential errors the $K\gamma$ is higher in the ESSP transmission, whereas for bigger tangential errors $K\gamma$ is higher in the ESIP transmissions.

Table 15: K_γ for ESIP 5-planet transmissions with tangential errors and 1e7 N/m stiffness in the sun

Error size (μm)	0	1.25	2.5	3.75	5	6.25
$K_{\gamma LSR}$	1	1.1505	1.301	1.451	1.6005	1.7485
$K_{\gamma SGLR_{su}}$	1	1.11	1.213	1.3155	1.4135	1.5095
$K_{\gamma SGLR_{ri}}$	1	1.0905	1.181	1.271	1.3615	1.4555

Table 16: K_γ for ESSP 5-planet transmissions with tangential errors and 1e7 N/m stiffness in the sun

Error size (μm)	0	1.25	2.5	3.75	5	6.25
$K_{\gamma LSR}$	1.142	1.2595	1.368	1.47	1.572	1.673
$K_{\gamma SGLR_{su}}$	1	1.105	1.21	1.3165	1.423	1.529
$K_{\gamma SGLR_{ri}}$	1	1.106	1.2005	1.294	1.3895	1.493

Finally, for the 1e6 N/m stiffness the results shown in Tab.17 & Tab.18 are almost identical to the ones in the 1e7 N/m stiffness scenario. Thus, the orbit cannot get bigger than the space between the sun and planet gear, and for the 1e6 N/m stiffness, the size of the orbit and, therefore, the variations in the LSR due to the stiffness in the sun support disappears. One notable fact regards the possibility of including a bigger tangential error without losing contact in the planet with the error. Finally, in the Fig.9 & Fig.10 these last results are graphed in order to see the trends followed by the $K\gamma$.

Table 17: K_γ for ESIP 5-planet transmissions with tangential errors and 1e6 N/m stiffness in the sun

Error size (μm)	0	1.25	2.5	3.75	5	6.25
$K_{\gamma LSR}$	1	1.151	1.3025	1.453	1.6035	1.752
$K_{\gamma SGLR_{su}}$	1	1.11	1.213	1.3155	1.4135	1.5095
$K_{\gamma SGLR_{ri}}$	1	1.091	1.1825	1.2735	1.3645	1.4555

Table 18: K_γ for ESSP 5-planet transmissions with tangential errors and 1e6 N/m stiffness in the sun

Error size (μm)	0	1.25	2.5	3.75	5	6.25
$K_{\gamma LSR}$	1.143	1.2605	1.37	1.473	1.5755	1.677
$K_{\gamma SGLR_{su}}$	1	1.1055	1.211	1.318	1.425	1.5315
$K_{\gamma SGLR_{ri}}$	1	1.106	1.2015	1.2955	1.3915	1.4955

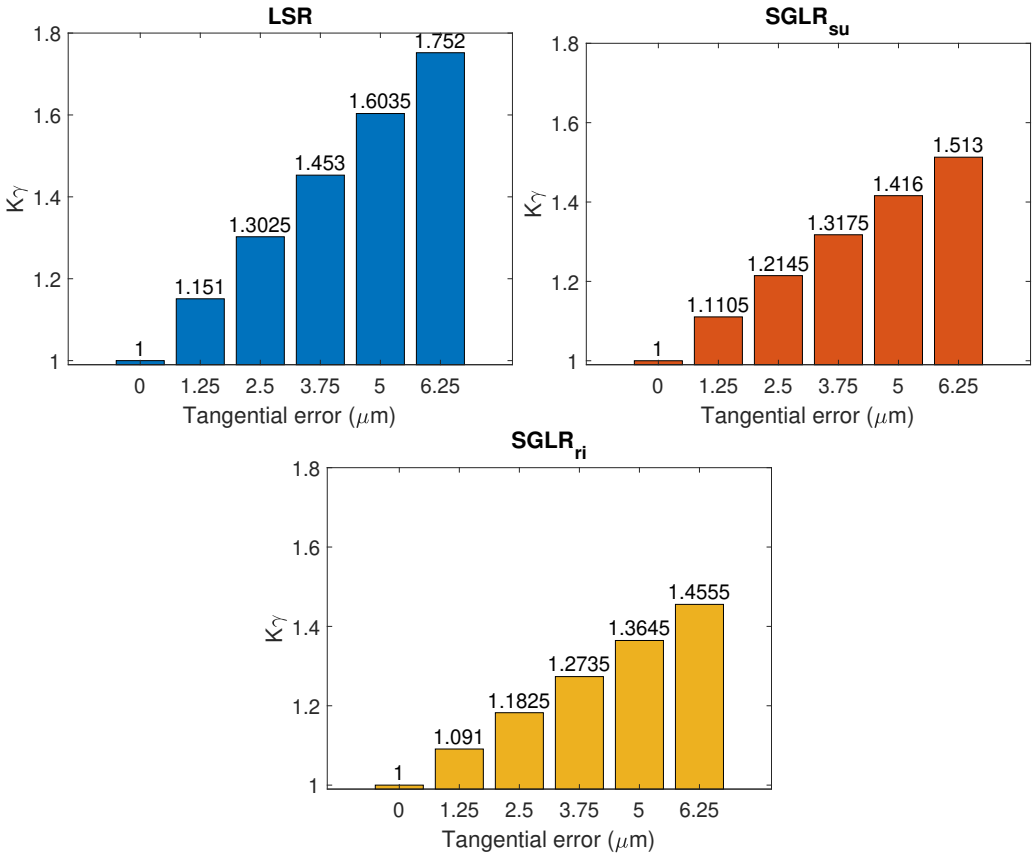

Figure 9: $K\gamma$ for 5-planet ESIP and 1e6 N/m stiffness in the sun support

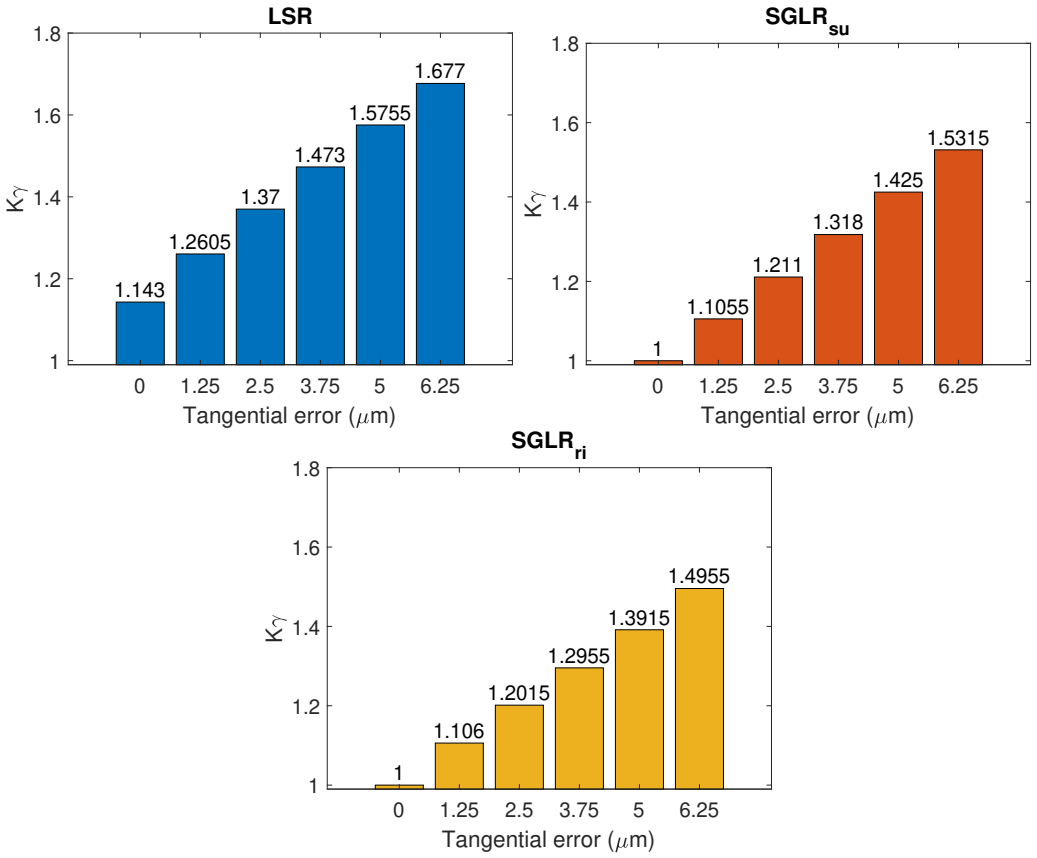

Figure 10: $K\gamma$ for 5-planet ESIP and 1e6 N/m stiffness in the sun support

A next step to take in the analysis consists in determining the differences between the $K_{\gamma LSR}$ & both $K_{\gamma SGLR}$. These are calculated employing eqn.8. These results provide the magnitude of the underestimation present in the measurement procedure employed to calculate the load sharing, at least for the studied scenarios which set a tendency from which conclusions can be extracted.

Those results are gathered in Tab.19 & Tab.20. These differences will be expressed as percentages, as seen in eqn.8, in order to represent the amount of load that is missed by the measurements with respect to the ideal load. These percentages are related to the ideal load value, represented by a $K\gamma$ of 1.

$$\Delta K_{\gamma SGLR} = (K_{\gamma LSR} - K_{\gamma SGLR}) \cdot 100 \tag{8}$$

Table 19: ΔK_γ for ESIP 5-planet transmission with various tangential errors and a 1e9 N/m stiffness

Stiffness (N/m)	1e9		1e8		1e7		1e6	
Error size (μm)	$\Delta K_{\gamma SGLR_{su}}$	$\Delta K_{\gamma SGLR_{ri}}$	$\Delta K_{\gamma SGLR_{su}}$	$\Delta K_{\gamma SGLR_{ri}}$	$\Delta K_{\gamma SGLR_{su}}$	$\Delta K_{\gamma SGLR_{ri}}$	$\Delta K_{\gamma SGLR_{su}}$	$\Delta K_{\gamma SGLR_{ri}}$
0	0	0	0	0	0	0	0	0
1.25	3.75	5.1	4.05	5.95	4.05	6	4.05	6
2.5	8.1	10.15	8.75	11.9	8.8	12	8.8	12
3.75	12.25	15.1	13.45	17.8	13.55	18	13.55	17.95
5			18.4	23.6	18.7	23.9	18.75	23.9
6.25							23.9	29.65

For ESIP transmissions (Tab.19), if there is no tangential pinhole position error the results of the measurements are accurate and ideal, as seen in [41]. Then, for any other scenario with variable sizes of tangential error, the measurements in the ring are less accurate than the ones in the sun, growing with the variation in the sun support stiffness. The difference between the real and measured load sharing grows with the tangential error, however, it grows more for the measurements in the ring gear. The amount of error in the measurements presented raises the concern with respect to the certification of a transmission. Besides, the load is underestimated and the underestimation seems to be considerably high, obviously with the limitations of the realism in the simulations.

Table 20: ΔK_γ for ESSP 5-planet transmission with various tangential errors and a 1e9 N/m stiffness

Stiffness (N/m)	1e9		1e8		1e7		1e6	
Error size (μm)	$\Delta K_{\gamma SGLR_{su}}$	$\Delta K_{\gamma SGLR_{ri}}$	$\Delta K_{\gamma SGLR_{su}}$	$\Delta K_{\gamma SGLR_{ri}}$	$\Delta K_{\gamma SGLR_{su}}$	$\Delta K_{\gamma SGLR_{ri}}$	$\Delta K_{\gamma SGLR_{su}}$	$\Delta K_{\gamma SGLR_{ri}}$
0	11	11	13.5	13.5	14.2	14.2	14.3	14.3
1.25	11.84	11.5	14.66	14.53	15.45	15.35	15.5	15.45
2.5	11.19	11.99	14.68	15.68	15.8	16.75	15.9	16.85
3.75	10.28	11.96	14.16	16.46	15.35	17.6	15.5	17.75
5			13.63	16.78	14.9	18.25	15.05	18.4
6.25					14.4	18	14.55	18.15

For the ESSP transmissions (Tab.20), there is an inherent error in the measurement, seen in the transmission without error. Then, the inaccuracy in the measurements in the sun shows the influence of the sun support stiffness. The $\Delta K\gamma$ grows initially but then decreases as the tangential error grows. This effect appears only in the measurements in the sun, which

proves the influence of the sun support stiffness which modifies the sun-planet meshing and the planet-ring meshing continues unmodified.

Aftwerwards, in order to deepen the analysis, these last data is represented in a couple of bar diagrams in Fig.11 & Fig.12, which allows to observe the tendencies in the results that have been commented above.

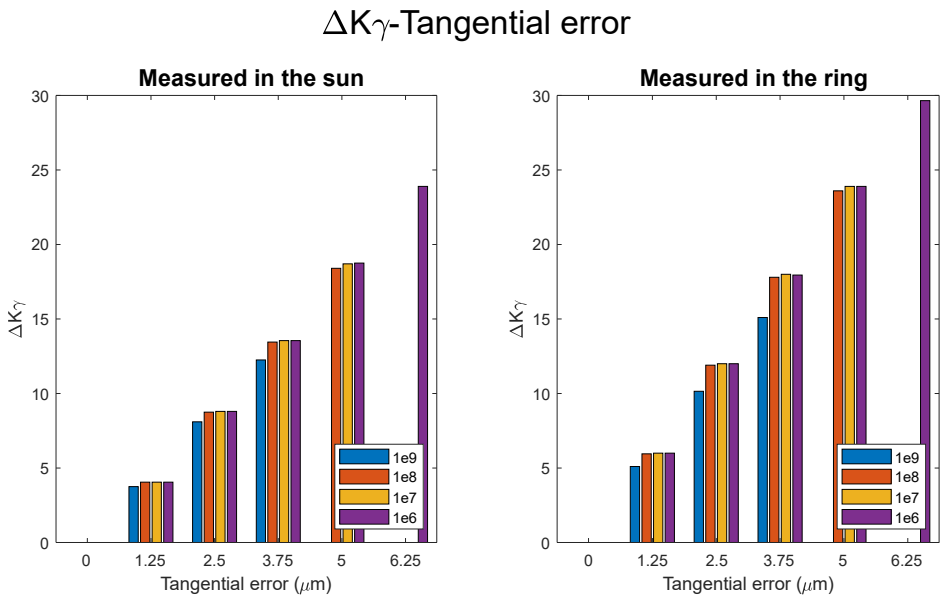

Figure 11: Real and measured $K\gamma$ for 5-planet ESIP with 3.75 tangential error

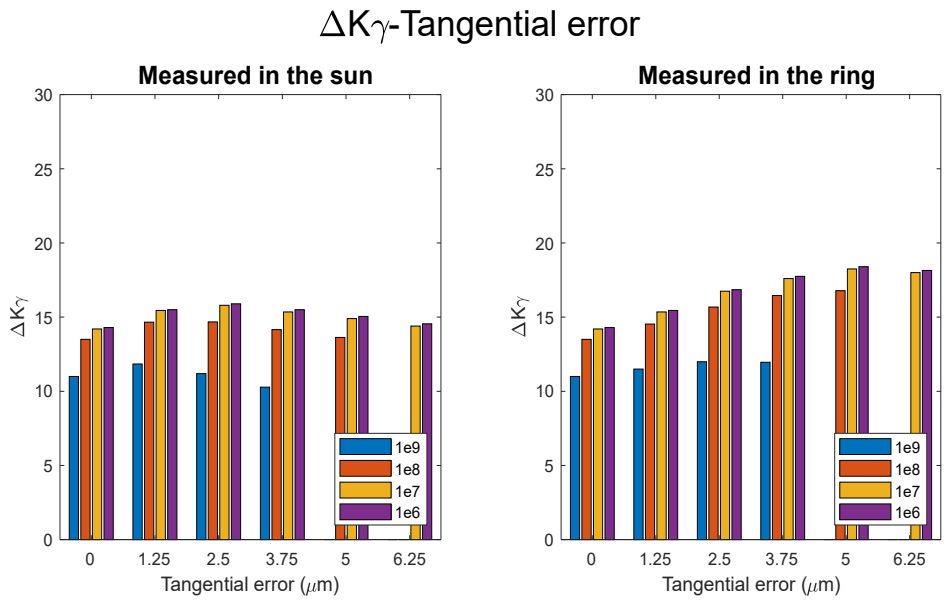

Figure 12: Real and measured $K\gamma$ for 5-planet ESSP with 3.75 tangential error

Finally, in order to extend the analysis, the results in K_γ for all the support stiffnesses and a 3.75 μm tangential error are gathered. This error is interesting, given that it is the biggest that is common to every of the considered scenarios. Taking these results, it is possible to see the comparison between the real and measured K_γ and the certification threshold set for a 5-planet transmission in wind generators. The Fig.13 & Fig.14 prove that the underestimation of the K_γ could affect the certification of the transmission, showing that the real K_γ crosses the threshold, which in the measured K_γ does not happen.

Comparing the results for ESIP and ESSP configurations, it is possible to see that the $K\gamma$, both real and measured, are higher in the ESSP configuration for the same working conditions.

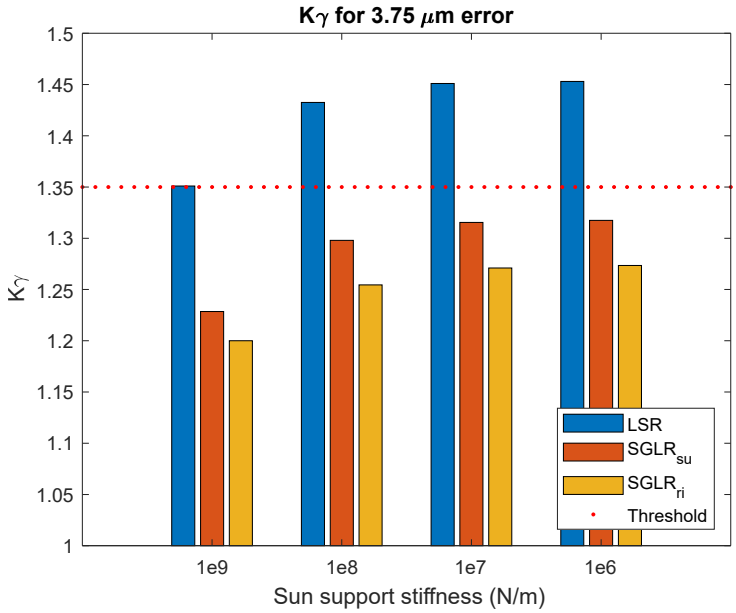

Figure 13: Real and measured $K\gamma$ for 5-planet ESIP with 3.75 tangential error

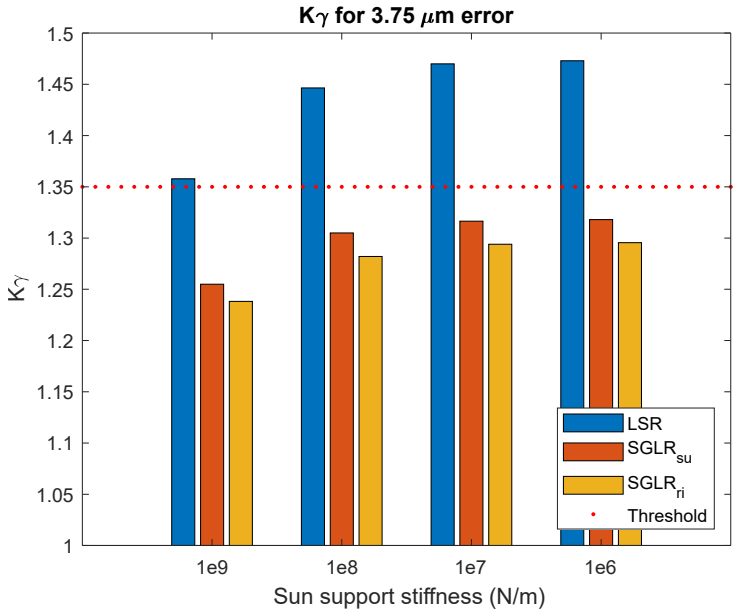

Figure 14: Real and measured $K\gamma$ for 5-planet ESSP with 3.75 tangential error

5. Conclusions

In this work a numerical study is presented in order to address the accuracy of the experimental measurement techniques in order to calculate the load sharing in a planetary transmission. This study is undergone using a semi-analytical model that provides the real and measured load sharing in various different scenarios. Thus, from the results already presented, it is possible to extract the following conclusions:

- The measurements both in the sun and ring gear underestimate the amount of load in the planets that set the mesh load factor in the transmission. Besides, the inclusion of floatability in the sun gear worsens this accuracy, specially in the ESIP transmissions.

- In ESIP configurations the measurements are more accurate than in the analogous ESSP transmission, however, this happens only for cases with a low or non-existing tangential error. As the size of the error grows, the measurements in the ESIP transmission becomes less accurate than in the ESSP transmission.

- The studied measurement techniques present an inherent error in ESSP transmissions, clearly affected by the sequence in the mesh phasing.

- The inaccuracy in the measurements grows with the tangential pinhole position in the ESIP transmission for both measurement techniques.

- For the measurements in the sun in ESSP transmission the inaccuracies in the measurements stays or diminishes with the size of the error. However, the inaccuracy grows with the floatability of the sun. On the other hand, the measurements in the ring gear under the same conditions grow in inaccuracy in all the studied scenarios.

6. Acknowledgements

The authors would like to acknowledge Project DPI2017-85390-P funded by the Spanish Ministry of Economy, Industry, and Competitiveness for supporting this research. Moreover, the authors acknowledge the Project PID2020-116213RB-I00 funded by the Ministry of Science and Innovation. Finally, the authors acknowledge SIEMENS-GAMESA for its collaboration in this work.

References

[1] W. Bartelmus and R. Zimroz, "A new feature for monitoring the condition of gearboxes in non-stationary operating conditions," *Mechanical Systems and Signal Processing*, vol. 23, pp. 1528–1534, jul 2009.

[2] W. Du, S. Zhao, L. Jin, J. Gao, and Z. Zheng, "Optimization design and performance comparison of different powertrains of electric vehicles," *Mechanism and Machine Theory*, vol. 156, p. 104143, 2021.

[3] J. Helsen, F. Vanhollebeke, F. De Coninck, D. Vandepitte, and W. Desmet, "Insights in wind turbine drive train dynamics gathered by validating advanced models on a newly developed 13.2MW dynamically controlled test-rig," *Mechatronics*, vol. 21, pp. 737–752, jun 2011.

[4] X. Liu, Y. Yang, and J. Zhang, "Resultant vibration signal model based fault diagnosis of a single stage planetary gear train with an incipient tooth crack on the sun gear," *Renewable Energy*, vol. 122, pp. 65–79, 2018.

[5] F. Viadero, A. Fernández, M. Iglesias, A. De-Juan, E. Liaño, and M. A. Serna, "Non-stationary dynamic analysis of a wind turbine power drivetrain: Offshore considerations," *Applied Acoustics*, vol. 77, pp. 204–211, 2014.

[6] J. I. Pedrero, D. Martínez-López, J. Calvo-Irisarri, M. Pleguezuelos, M. B. Sánchez, and A. Fernández-Sisón, "Minimum friction losses in wind turbine gearboxes," *Forschung im Ingenieurwesen/Engineering Research*, 2021.

[7] L. Antolick, J. Branning, D. Wade, and P. Dempsey, "Evaluation of gear condition indicator performance on rotorcraft fleet," in *Annual Forum Proceedings - AHS International*, vol. 2, pp. 1110–1121, 2010.

[8] M. Botman, "Vibration measurements on planetary gears of aircraft turbine engines," *Journal of Aircraft*, vol. 17, no. 5, pp. 351–357, 1980.

[9] A. Kahraman, "Load sharing characteristics of planetary transmissions," *Mechanism and Machine Theory*, vol. 29, no. 8, pp. 1151–1165, 1994.

[10] A. Kahraman, "Natural Modes of Planetary Gear Trains," *Journal of Sound and Vibration*, vol. 173, pp. 125–130, may 1994.

[11] A. Saada and P. Velex, "An Extended Model for the Analysis of the Dynamic Behavior of Planetary Trains," *Journal of Mechanical Design*, vol. 117, pp. 241–247, jun 1995.

[12] M. B. Sánchez, M. Pleguezuelos, and J. I. Pedrero, "Influence of profile modifications on meshing stiffness, load sharing, and trasnsmission error of involute spur gears," *Mechanism and Machine Theory*, vol. 139, pp. 506–525, 2019.

[13] M. Pleguezuelos, M. B. Sánchez, and J. I. Pedrero, "Analytical model for meshing stiffness, load sharing, and transmission error for spur gears with profile modification under non-nominal load conditions," *Applied Mathematical Modelling*, vol. 97, pp. 344–365, 2021.

[14] Z. Chen, Z. Zhou, W. Zhai, and K. Wang, "Improved analytical calculation model of spur gear mesh excitations with tooth profile deviations," *Mechanism and Machine Theory*, vol. 149, p. 103838, 2020.

[15] L. Ryali and D. Talbot, "A dynamic load distribution model of planetary gear sets," *Mechanism and Machine Theory*, vol. 158, p. 104229, apr 2021.

[16] Y. Hu, D. Talbot, and A. Kahraman, "A Load Distribution Model for Planetary Gear Sets," *Journal of Mechanical Design*, vol. 140, no. 5, p. 053302, 2018.

[17] H. Dai, X. Long, F. Chen, and C. Xun, "An improved analytical model for gear mesh stiffness calculation," *Mechanism and Machine Theory*, vol. 159, p. 104262, 2021.

[18] V. Abousleiman and P. Velex, "A hybrid 3D finite element/lumped parameter model for quasi-static and dynamic analyses of planetary/epicyclic gear sets," *Mechanism and Machine Theory*, vol. 41, no. 6, pp. 725–748, 2006.

[19] J. Helsen, F. Vanhollebeke, B. Marrant, D. Vandepitte, and W. Desmet, "Multibody modelling of varying complexity for modal behaviour analysis of wind turbine gearboxes," *Renewable Energy*, vol. 36, pp. 3098–3113, nov 2011.

[20] V. Abousleiman, P. Velex, and S. Becquerelle, "Modeling of spur and helical gear planetary drives with flexible ring gears and planet carriers," *Journal of Mechanical Design, Transactions of the ASME*, vol. 129, no. 1, pp. 95–106, 2007.

[21] J. T. Kahnamouei and J. Yang, "Development and verification of a computationally efficient stochastically linearized planetary gear train model with ring elasticity," *Mechanism and Machine Theory*, vol. 155, 2021.

[22] M. Iglesias, A. Fernandez del Rincon, A. De-Juan, A. Diez-Ibarbia, P. Garcia, and F. Viadero, "Advanced model for the calculation of meshing forces in spur gear planetary transmissions," *Meccanica*, vol. 50, no. 7, pp. 1869–1894, 2015.

[23] T. Barszcz and R. B. Randall, "Application of spectral kurtosis for detection of a tooth crack in the planetary gear of a wind turbine," *Mechanical Systems and Signal Processing*, vol. 23, pp. 1352–1365, may 2009.

[24] K. Feng, W. A. Smith, R. B. Randall, H. Wu, and Z. Peng, "Vibration-based monitoring and prediction of surface profile change and pitting density in a spur gear wear process," *Mechanical Systems and Signal Processing*, vol. 165, p. 108319, feb 2022.

[25] D. Peng, W. A. Smith, R. B. Randall, and Z. Peng, "Use of mesh phasing to locate faulty planet gears," *Mechanical Systems and Signal Processing*, vol. 116, pp. 12–24, 2019.

[26] N. Mokhtari, M. Grzeszkowski, and C. Gühmann, "Vibration signal analysis for the lifetime-prediction and failure detection of future turbofan components," *Technische Mechanik*, vol. 37, no. 2-5, pp. 422–431, 2017.

[27] E. Caso, A. Fernandez-del Rincon, P. Garcia, M. Iglesias, and F. Viadero, "Monitoring of misalignment in low speed geared shafts with acoustic emission sensors," *Applied Acoustics*, vol. 159, p. 107092, feb 2020.

[28] P. Garcia Fernandez, A. De-Juan, A. Diez-Ibarbia, J. Sanchez-Espiga, and A. Fernandez del Rincon, "Acoustic intensity technique applied to monitor planetary gears," *Applied Acoustics*, vol. 172, 2021.

[29] R. Fargère and P. Velex, "Some experimental and simulation results on the dynamic behaviour of spur and helical geared transmissions with journal bearings," *Advances in Tribology*, vol. 2012, pp. 1–9, 2012.

[30] X. Dai, C. G. Cooley, and R. G. Parker, "Dynamic tooth root strains and experimental correlations in spur gear pairs," *Mechanism and Machine Theory*, no. 101, pp. 60–74, 2016.

[31] M. Guingand, J. P. de Vaujany, and C. Y. Jacquin, "Quasi-static analysis of a face gear under torque," *Computer Methods in Applied Mechanics and Engineering*, vol. 194, no. 39-41, pp. 4301–4318, 2005.

[32] H. Aurrekoetxea and I. R. D. Ocenda, "Experimental and theoretical study of load mesh factor for different boundary conditions in wind gearbox planetary stages," in *International Conference on Gears 2019*, pp. 835–844, VDI Verlag, 2019.

[33] H. Ligata, A. Kahraman, and A. Singh, "A Closed-Form Planet Load Sharing Formulation for Planetary Gear Sets Using a Translational Analogy," *Journal of Mechanical Design*, vol. 131, no. 2, p. 021007, 2009.

[34] A. Kahraman, "Static Load Sharing Characteristics of Transmission Planetary Gear Sets : Model and Experiment," *Transmission and Driveline Systems Symposium*, no. 1, pp. 1–10, 1999.

[35] M.-C. Noll, J. W. Godfrey, R. Schelenz, and G. Jacobs, "Analysis of time-domain signals of piezoelectric strain sensors on slow spinning planetary gearboxes," *Mechanical Systems and Signal Processing*, vol. 72-73, pp. 727–744, may 2016.

[36] J.-g. Kim, Y.-j. Park, G.-h. Lee, and J.-h. Kim, "An Experimental Study on the Effect of Carrier Pinhole Position Errors on Planet Gear Load Sharing," vol. 17, no. 10, pp. 1305–1312, 2016.

[37] J. Götz, F. Siglmüller, M. Fürst, M. Otto, and K. Stahl, "Experimental investigation of the dynamic load sharing of planetary gearboxes," *Forschung im Ingenieurwesen*, jul 2021.

[38] B. Boguski, A. Kahraman, and T. Nishino, "A New Method to Measure Planet Load Sharing and Sun Gear Radial Orbit of Planetary Gear Sets," *Journal of Mechanical Design*, vol. 134, no. 7, p. 071002, 2012.

[39] L. Ryali, A. Verma, I. Hong, D. Talbot, and F. Zhu, "Experimental and theoretical investigation of quasi-static system level behavior of planetary gear sets," *Journal of Mechanical Design, Transactions of the ASME*, vol. 143, no. 10, 2021.

[40] "IEC61400 – 4: Design Requirements for wind turbine gearboxes."

[41] J. Sanchez-Espiga, A. Fernandez-del Rincon, M. Iglesias, and F. Viadero, "Planetary gear transmissions load sharing measurement from tooth root strains: Numerical evaluation of mesh phasing influence," *Mechanism and Machine Theory*, vol. 163, p. 104370, sep 2021.

[42] A. Bodas and A. Kahraman, "Influence of Carrier and Gear Manufacturing Errors on the Static Load Sharing Behavior of Planetary Gear Sets," *JSME International Journal Series C*, vol. 47, no. 3, pp. 908–915, 2004.

[43] J. Sanchez-Espiga, A. Fernandez-del Rincon, M. Iglesias, and F. Viadero, "Influence of errors in planetary transmissions load sharing under different mesh phasing," *Mechanism and Machine Theory*, vol. 153, p. 104012, nov 2020.

[44] H. Ligata, A. Kahraman, and A. Singh, "An Experimental Study of the Influence of Manufacturing Errors on the Planetary Gear Stresses and Planet Load Sharing," *Journal of Mechanical Design*, vol. 130, no. 4, p. 041701, 2008.

[45] M. Iglesias, A. Fernandez del Rincon, A. De-Juan, P. Garcia, A. Diez-Ibarbia, and F. Viadero, "Planetary transmission load sharing: Manufacturing errors and system configuration study," *Mechanism and Machine Theory*, vol. 111, pp. 21–38, 2017.

[46] ISO, "ISO 6336 - Calculation of load capacity of spur and helical gears - Application for industrial gears," no. 1, 1996.

[47] J. I. Pedrero, M. Pleguezuelos, and M. B. Sánchez, "Influence of meshing stiffness on load distribution between planets of planetary gear drives," *Mechanism and Machine Theory*, vol. 170, no. November 2021, 2022.